View metadata, citation and similar papers at core.ac.uk

brought to you by CORE

provided by epublications@Marquette

Marquette University
e-Publications@Marquette

Biomedical Engineering Faculty Research and Publications

Biomedical Engineering, Department of

6-1-2016

Evaluating Descriptive Metrics of the Human Cone Mosaic

Robert F. Cooper
Marquette University

Melissa A. Wilk
Medical College of Wisconsin

Sergey Tarima
Medical College of Wisconsin

Joseph Carroll
Marquette University

Published Version. *Investigative Ophthalmology & Visual Science,* Vol. 57, No. 7 (June 2016): 2992-3001. DOI. © 2016 Association for Research in Vision and Ophthalmology. Used with permission.

Evaluating Descriptive Metrics of the Human Cone Mosaic

Robert F. Cooper,[*,1] Melissa A. Wilk,[2] Sergey Tarima,[3] and Joseph Carroll[1,2,4,5]

[1]Biomedical Engineering, Marquette University, Milwaukee, Wisconsin, United States
[2]Cell Biology, Neurobiology and Anatomy, Medical College of Wisconsin, Milwaukee, Wisconsin, United States
[3]Biostatistics, Institute for Health and Society, Medical College of Wisconsin, Milwaukee, Wisconsin, United States
[4]Biophysics, Medical College of Wisconsin, Milwaukee, Wisconsin, United States
[5]Ophthalmology, Medical College of Wisconsin, Milwaukee, Wisconsin, United States

Correspondence: Joseph Carroll, Eye Institute, Department of Ophthalmology, Medical College of Wisconsin, 925 N 87th Street, Milwaukee, WI 53226-0509, USA; jcarroll@mcw.edu.

Current affiliation: *Departments of Ophthalmology and Psychology, University of Pennsylvania, Philadelphia, Pennsylvania, United States.

Submitted: January 4, 2016
Accepted: April 10, 2016

Citation: Cooper RF, Wilk MA, Tarima S, Carroll J. Evaluating descriptive metrics of the human cone mosaic. *Invest Ophthalmol Vis Sci*. 2016;57:2992–3001. DOI:10.1167/iovs.16-19072

Purpose. To evaluate how metrics used to describe the cone mosaic change in response to simulated photoreceptor undersampling (i.e., cell loss or misidentification).

Methods. Using an adaptive optics ophthalmoscope, we acquired images of the cone mosaic from the center of fixation to 10° along the temporal, superior, inferior, and nasal meridians in 20 healthy subjects. Regions of interest ($n = 1780$) were extracted at regular intervals along each meridian. Cone mosaic geometry was assessed using a variety of metrics – density, density recovery profile distance (DRPD), nearest neighbor distance (NND), intercell distance (ICD), farthest neighbor distance (FND), percentage of six-sided Voronoi cells, nearest neighbor regularity (NNR), number of neighbors regularity (NoNR), and Voronoi cell area regularity (VCAR). The "performance" of each metric was evaluated by determining the level of simulated loss necessary to obtain 80% statistical power.

Results. Of the metrics assessed, NND and DRPD were the least sensitive to undersampling, classifying mosaics that lost 50% of their coordinates as indistinguishable from normal. The NoNR was the most sensitive, detecting a significant deviation from normal with only a 10% cell loss.

Conclusions. The robustness of cone spacing metrics makes them unsuitable for reliably detecting small deviations from normal or for tracking small changes in the mosaic over time. In contrast, regularity metrics are more sensitive to diffuse loss and, therefore, better suited for detecting such changes, provided the fraction of misidentified cells is minimal. Combining metrics with a variety of sensitivities may provide a more complete picture of the integrity of the photoreceptor mosaic.

Keywords: adaptive optics, photoreceptors, modeling, cone mosaic

Adaptive optics (AO) enhanced ophthalmoscopes permit noninvasive visualization of the human retina with cellular resolution. Imaging of the cone,[1–5] rod,[6–8] and retinal pigment epithelium (RPE)[9–13] mosaics has been demonstrated in healthy and diseased eyes. While pathology can often be quite striking when imaged with single-cell resolution, the ability to use these images to detect subtle changes relies on the ability to extract quantitative information about the mosaic of interest. This process often involves assessing metrics derived from the cell locations within an image. Metrics such as density,[14–24] spacing,[12,14,15,23,25–31] and regularity[19,32–34] are frequently used to characterize the cone mosaic. Despite their broad use, there has been minimal evaluation of the ability of these metrics to detect disruptions of the photoreceptor mosaic. Such testing is needed to objectively assess the strengths and weaknesses of these metrics in evaluating retinal mosaics, especially with the growing demand to image the photoreceptor mosaic over time (either following therapeutic intervention or to monitor disease progression).

One of the more significant factors known to affect metrics used to describe the cone mosaic is undersampling. Undersampling can come from two sources: cell misidentification or cell loss.[35,36] First, algorithms used to automatically or semiautomatically identify cells in retinal mosaics have some nonnegligible errors that can vary substantially with image quality.[14,15,34] As most metrics rely on cell identification rather than the retinal image itself (though Cooper et al.[37] uses a Fourier transform-derived spacing extracted directly from the image), the error introduced by this undersampling is an inherent feature of most current AO analyses. How this source of undersampling affects a given metric provides a direct measure of its "robustness." Second, various retinal diseases result in the actual loss of cells from the mosaic.[21,22,25,29–33,38–42] How a metric changes in response to known amounts of cell loss defines its "sensitivity." As there is a wide range of metrics used to assess retinal mosaics, it is critical to characterize how each metric is affected by undersampling: an ideal metric should be sensitive enough to detect cell loss, but robust enough to not be affected by small errors in cell identification.

Due in part to the optical waveguiding properties of photoreceptors, the cone mosaic can be imaged with particular ease. In fact, the cone mosaic can be resolved in some individuals even without using AO.[43–46] Moreover, cone photoreceptors drive the majority of our visual function and are affected in a variety of retinal diseases. Thus, there is continued interest in the development and validation of metrics for detecting disruptions or changes in the cone mosaic. Following the approach developed by Cook,[35] in which he compared versions of the

This work is licensed under a Creative Commons Attribution-NonCommercial-NoDerivatives 4.0 International License.

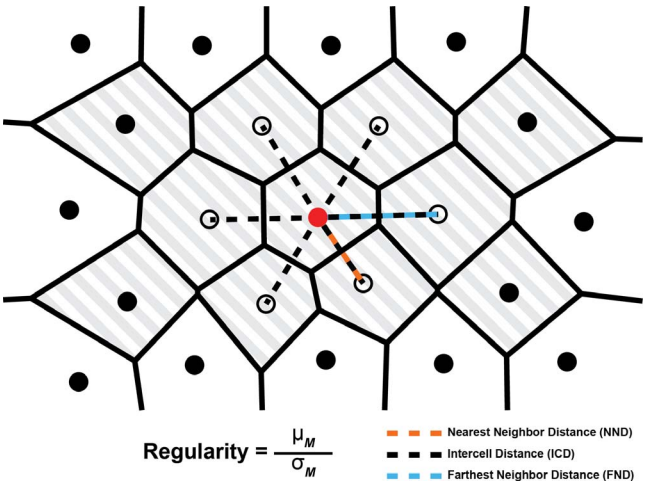

FIGURE 1. A schematic of a hexagonally arranged patch of cones illustrating the relationship between the distance measurements used in this study. A single cone (*red circle*) and its six closest neighbors (*open circles*) are highlighted for clarity. The NND is defined as the distance from a given cone to its closest neighbor (*orange dashed line*). The FND is defined as the distance from each cone to its most distant neighbor (*blue dashed line*), and ICD is defined as the average distance between a cone and all of its neighbors (*dashed lines*). In order to mitigate boundary effects, only cones with bound Voronoi regions (*shaded region*) are included when calculating each metric. The regularity of each of these metrics (*M*) is defined as the mean (μ_M) of the metric for all cones with bounded Voronoi cells, divided by the metric's SD (σ_M).

same mosaic that had different amounts of undersampling, we examined the performance of a number of metrics by applying known amounts of diffuse cell loss (i.e., undersampling) to photoreceptor mosaic coordinates derived from images of the human cone mosaic. This pattern of cone mosaic disruption has been observed in conditions such as retinitis pigmentosa,[25,41] cone-rod dystrophy,[25] red-green color vision deficiency,[38] and acute macular neuroretinopathy.[22] In addition, this type of undersampling approximates the expected pattern that might occur as a result of errors in manual or automated cell detection. The data presented here provide a useful framework for understanding the strengths and limitations of these metrics, and highlight the important "philosophical" issue of whether the insensitivity (or robustness) of a metric to diffuse cell loss represents a strength or a weakness when trying to determine whether a given cone mosaic is normal or abnormal.

METHODS

Human Subjects

This research followed the tenets of the Declaration of Helsinki, and was approved by the institutional review boards at the Medical College of Wisconsin (Milwaukee, WI, USA) and Marquette University (Milwaukee, WI, USA). Twenty subjects with normal trichromatic vision were recruited for this study (median age: 23.5, range, 9–67 years; Supplementary Table S1). Subjects provided informed consent after the nature and possible consequences of the study were explained. Individuals with high myopia or hyperopia (>10 diopters [D]) were excluded from this study. Axial length measurements were obtained on all subjects using an IOL Master (Carl Zeiss Meditec, Dublin, CA, USA). To convert from image pixels to retinal distance (μm), we first acquired images of a Ronchi ruling positioned at the focal plane of a lens with a 19-mm focal length to determine the conversion between image pixels and degrees. An adjusted axial length method[47] was then used to approximate the retinal magnification factor (in μm/degree) and convert to micrometer per pixel.

Imaging the Human Photoreceptor Mosaic

The photoreceptor mosaic was imaged using an AO scanning light ophthalmoscope (AOSLO), where both confocal[48] and nonconfocal split-detector[1] imaging modalities were acquired simultaneously. Imaging was performed along the temporal, inferior, nasal, and superior meridians using a 790-nm superluminescent diode. Using a 1.0° field of view (FOV), each meridian was sampled every half degree from fixation out to 6°, and then every degree from 7° to 10°. Using a 1.5° FOV, each meridian was sampled every degree from fixation out to 10°. To correct for static intraframe distortion resulting from the sinusoidal motion of the resonant optical scanner, we estimated the distortion from images of a stationary Ronchi ruling and then resampled each frame over a grid of equally spaced pixels. Then, a reference frame was selected manually from within each image sequence for subsequent registration using custom software.[49] Montages of overlapping split-detector and confocal images using both 1.0° and 1.5° FOVs were created semiautomatically using custom software. To simplify the process of montaging, custom software was created in MATLAB (Mathworks, Natick, MA, USA) that allows the user to rapidly screen which images should be included in a montage. After screening, the selected images were automatically placed in a corresponding Photoshop (Adobe, San Jose, CA, USA) file at a location extracted from the digitized image acquisition notes. Once the montage was "seeded" using this software, the user manually positioned the images within Photoshop to achieve a more accurate alignment.

Analyzing the Cone Photoreceptor Mosaic

Because foveal cones could not be reliably resolved in all subjects, the location of peak foveal density was determined using a previously described method.[50] First, cone coordinates were semiautomatically identified from a foveal montage using a previously described cell identification algorithm.[15] Isodensity contour maps were generated from the resulting coordinates. Six contours (at 80%–93% of the peak cone density) were extracted from each map, and the center (x, y) position of each contour was averaged to provide an estimate of the location of peak foveal cone density within the foveal montage.

Regions of interest (ROIs) were then extracted from each montage, relative to the location of peak foveal cone density, using custom software (Photoshop and MATLAB). The size of each ROI varied as a function of eccentricity, using published AOSLO-derived cone density data[51] to estimate the area necessary to encompass approximately 100 cones at each ROI as described next. Using the minimum foveal cone density observed by Wilk et al.[51] (84,000 cones/mm^2), we set the area of ROIs at the location of peak foveal cone density to 37 × 37 μm. Due to the minimal change in cone density beyond 10°, we set the area of ROIs at and beyond 10° to 100 × 100 μm. We next fit an exponential function to these areas, establishing an eccentricity-to-ROI area relationship. We obtained ROIs at the foveal center, every 50 μm from 50- to 600-μm eccentricity, every 200 μm from 600- to 1600-μm eccentricity, and every 300 μm from 1600- to 3100-μm eccentricity. Within 500 μm of peak foveal cone density, ROIs were extracted from the confocal modality, while beyond 500 μm, ROIs were extracted from the split-detector modality due to superior cone contrast. When either blood vessels or seams between overlapping images occurred at a desired ROI sampling location, we

Investigative Ophthalmology & Visual Science

Table. The Intersubject Mean (±SD) of Each Metric as a Function of Eccentricity

Eccentricity Bin, μm	Density, Cones/mm²	NND, μm	DRPD, μm	ICD, μm	FND, μm	% 6-Sided	VCAR	NoNR	NNR
0	119,000 ± 23,300	2.43 ± 0.24	3.10 ± 0.37	3.15 ± 0.38	3.98 ± 0.53	54.8 ± 10.9	3.70 ± 1.07	7.88 ± 1.40	8.37 ± 1.38
50	114,000 ± 20,200	2.56 ± 0.23	3.28 ± 0.34	3.27 ± 0.32	4.06 ± 0.45	62.9 ± 12.2	6.16 ± 0.85	9.39 ± 2.32	8.35 ± 1.14
100	104,000 ± 17,000	2.69 ± 0.24	3.50 ± 0.35	3.41 ± 0.31	4.19 ± 0.42	69.0 ± 10.2	6.57 ± 1.04	10.4 ± 2.06	8.57 ± 1.30
150	87,600 ± 13,400	2.94 ± 0.19	3.82 ± 0.29	3.71 ± 0.31	4.50 ± 0.43	70.9 ± 9.56	7.13 ± 1.22	10.9 ± 2.02	8.98 ± 1.46
200	75,400 ± 10,700	3.20 ± 0.18	4.08 ± 0.26	3.98 ± 0.28	4.81 ± 0.38	71.2 ± 8.99	7.68 ± 1.23	11.1 ± 1.95	9.41 ± 1.41
250	65,900 ± 9,410	3.38 ± 0.20	4.33 ± 0.27	4.27 ± 0.30	5.17 ± 0.39	67.4 ± 9.47	7.85 ± 1.35	10.3 ± 1.85	9.56 ± 1.54
300	58,400 ± 9,390	3.57 ± 0.22	4.55 ± 0.29	4.54 ± 0.37	5.55 ± 0.52	64.4 ± 9.73	7.88 ± 1.50	9.84 ± 1.68	9.55 ± 1.65
350	52,200 ± 9,300	3.78 ± 0.33	4.73 ± 0.32	4.83 ± 0.47	5.93 ± 0.65	61.5 ± 9.00	7.90 ± 1.65	9.32 ± 1.45	9.71 ± 1.79
400	46,200 ± 9,930	3.92 ± 0.29	4.94 ± 0.39	5.17 ± 0.65	6.29 ± 0.65	58.0 ± 8.38	7.76 ± 1.85	8.82 ± 1.35	9.48 ± 2.14
450	42,700 ± 10,100	4.20 ± 0.43	5.01 ± 0.38	5.39 ± 0.65	6.58 ± 0.63	57.2 ± 7.28	7.56 ± 1.69	8.60 ± 1.08	9.51 ± 2.09
500	38,900 ± 6,630	4.39 ± 0.33	5.17 ± 0.33	5.59 ± 0.49	6.97 ± 0.68	54.8 ± 5.75	7.25 ± 1.59	8.29 ± 0.84	9.10 ± 2.12
550	34,700 ± 8,450	4.54 ± 0.47	5.36 ± 0.55	5.88 ± 0.64	7.35 ± 0.83	52.9 ± 6.08	6.92 ± 1.69	7.92 ± 0.88	8.59 ± 2.05
600	31,500 ± 8,090	4.72 ± 0.46	5.50 ± 0.55	6.15 ± 0.64	7.72 ± 0.83	52.5 ± 6.10	7.00 ± 1.79	7.95 ± 0.84	8.55 ± 2.22
800	24,200 ± 5,860	5.46 ± 0.71	6.40 ± 0.96	7.18 ± 0.90	9.01 ± 1.21	51.8 ± 6.55	6.93 ± 1.60	7.85 ± 0.82	7.64 ± 1.63
1000	20,100 ± 5,110	5.98 ± 0.78	7.15 ± 1.21	7.85 ± 0.93	9.85 ± 1.22	52.6 ± 6.56	6.96 ± 1.45	7.92 ± 0.95	7.59 ± 1.21
1200	16,400 ± 3,140	6.60 ± 0.70	7.82 ± 1.27	8.61 ± 0.78	10.8 ± 1.02	54.5 ± 6.09	7.18 ± 1.44	8.08 ± 0.90	7.86 ± 1.32
1400	15,100 ± 2,450	6.87 ± 0.60	8.31 ± 1.05	8.95 ± 0.76	11.2 ± 1.09	54.1 ± 5.85	7.45 ± 1.43	8.11 ± 0.84	7.87 ± 1.23
1600	13,100 ± 2,080	7.35 ± 0.56	9.09 ± 0.86	9.56 ± 0.78	12.0 ± 1.14	53.2 ± 6.64	7.52 ± 1.56	7.96 ± 0.84	8.33 ± 1.27
1900	11,900 ± 1,960	7.73 ± 0.60	9.38 ± 0.89	10.1 ± 0.88	12.6 ± 1.40	53.4 ± 7.10	7.59 ± 1.48	8.05 ± 0.89	8.30 ± 1.21
2200	10,400 ± 1,610	8.19 ± 0.56	10.1 ± 1.00	10.7 ± 0.79	13.4 ± 1.15	50.9 ± 7.32	7.62 ± 1.60	7.80 ± 0.74	8.20 ± 1.20
2500	9,570 ± 1,390	8.48 ± 0.60	10.5 ± 1.11	11.2 ± 0.80	14.0 ± 1.11	50.3 ± 7.19	7.46 ± 1.50	7.56 ± 0.89	8.02 ± 1.21
2800	8,780 ± 1,280	8.83 ± 0.59	11.0 ± 1.12	11.6 ± 0.80	14.6 ± 1.18	49.0 ± 8.52	7.27 ± 1.35	7.53 ± 0.94	7.72 ± 1.10
3100	7,960 ± 1,310	9.21 ± 0.68	11.4 ± 1.39	12.2 ± 1.02	15.4 ± 1.59	48.6 ± 7.65	7.02 ± 1.50	7.42 ± 0.92	7.64 ± 1.10

NND, nearest neighbor distance; DRPD, density recovery profile distance; ICD, intercell distance; FND, farthest neighbor distance; VCAR, Voronoi cell area regularity; NoNR, number of neighbors regularity; NNR, nearest neighbor regularity.

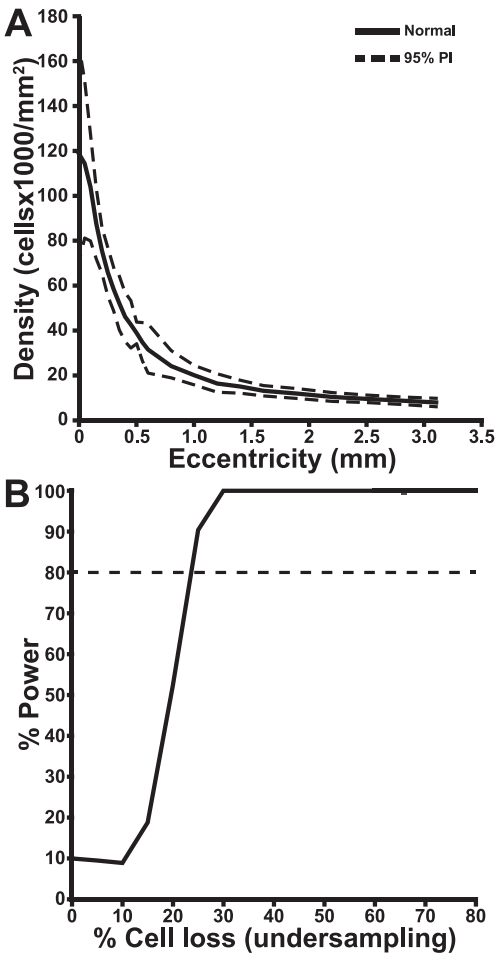

FIGURE 2. Assessing the sensitivity of cone density to varying amounts of cell loss. (**A**) The mean of all 20 subjects' density as a function of eccentricity (*solid line*) with the 95% prediction interval (*dashed lines*). (**B**) The statistical power curve for cone density (*solid line*) does not reach the 80% threshold (*horizontal dashed line*) until a 24% cone undersampling, implying that density cannot reliably detect an abnormal cone mosaic until greater than 24% of the cells have been lost.

adjusted the ROI's location to a nearby unobstructed area. To enable easier comparison, each ROI was binned based on the nearest sample location. Regions of interest within an eccentricity bin were then compared across all subjects. On average, the ROIs deviated from their bin location by 4.7 μm within 600 μm of the foveal center, and 67.4 μm beyond 600 μm from the foveal center. Cone coordinates were then semiautomatically identified within each confocal ROI,[15] and manually identified within each split-detector ROI using custom software (Java 1.8; Oracle, Redwood City, CA, USA) by a single observer (RFC).

Mitigation of Boundary Effects

All geometrical descriptors extracted from a discrete set of coordinates are subject to boundary effects at the ROI edges. The edge cells do not necessarily contribute all of their connected neighbors to a spacing measurement, or even all of the area that they encompass to a density measurement. To mitigate this effect, we used the Voronoi tessellation to establish which cell locations should be included for analysis. Only cones with their corresponding Voronoi cell fully contained within the ROI (i.e., "bound") were considered for the metric calculations.

Descriptive Metrics of the Cone Mosaic

The cone coordinates for each ROI were analyzed using the following spacing and regularity metrics (regularity metrics, as the name implies, capture the variation of a particular metric over an ROI):

Density. As mentioned above, Voronoi tessellation of the cone coordinates was used to define the bound Voronoi cells in a given ROI. Density was defined as the ratio of the number of bound Voronoi cells in an ROI to the summed area of the bound Voronoi cells. The shaded Voronoi polygons in Figure 1 represent bound Voronoi cells.

Percent Six-Sided Voronoi Cells. The number of sides of each bound Voronoi cell was determined, and the number of Voronoi cells with six sides was divided by the total number of bound Voronoi cells within an ROI.

Density Recovery Profile Distance (DRPD). The density recovery profile (DRP) is a method based on a two-dimensional autocorrelogram that is an expression of the spatial density of cells as a function of the distance of each cell from all other cells.[26,36] To automatically determine spacing from the DRP, we first determined the width of each bin as defined by equation 16 in Rodieck et al.,[36] assuming a reliability of two. After calculating the DRP, we interpolated between each bin using splines. We then found the first local maximum within the spline that was greater than the DRP density mean. The *x*-axis location (distance) of the maximum was taken as the DRPD.

Nearest Neighbor Distance (NND). The distance between a given cone and its closest neighbor, where the neighbors of a given cone are comprised of all cones with adjacent Voronoi cells. The NND reported for each ROI is the average NND for all of the cones with bound Voronoi cells in that ROI (Fig. 1, orange dashed line).

Intercell Distance (ICD). The average distance between a given cone and each of its neighbors, where the neighbors of a given cone are comprised of all cones with adjacent Voronoi cells. The ICD reported for each ROI is the average ICD for all of the cones with bound Voronoi cells in that ROI (Fig. 1, black dashed lines).

Farthest Neighbor Distance (FND). The distance between a given cone and its farthest neighbor, where the neighbors of a given cone are comprised of all cones with adjacent Voronoi cells. The FND reported for each ROI is the average FND for all of the cones with bound Voronoi cells in that ROI (Fig. 1, blue dashed line).

Nearest Neighbor Regularity (NNR). The mean nearest neighbor distance (NND) for all of the cones with bound Voronoi cells in an ROI divided by the standard deviation (SD) of the NND for all of the cones with bound Voronoi cells in that ROI.

Number of Neighbors Regularity (NoNR). The mean number of sides of all bound Voronoi cells in an ROI divided by the SD of the number of sides of all bound Voronoi cells in that ROI.

Voronoi Cell Area Regularity (VCAR). The mean area of the bound Voronoi cells in an ROI divided by the SD of the area of the bound Voronoi cells in that ROI.

Examining the Sensitivity of Metrics to Undersampling

After calculating each metric from each normal ROI, we used a statistical classifier to determine the threshold at which a metric could sensitively detect diffuse loss. To create the

Investigative Ophthalmology & Visual Science

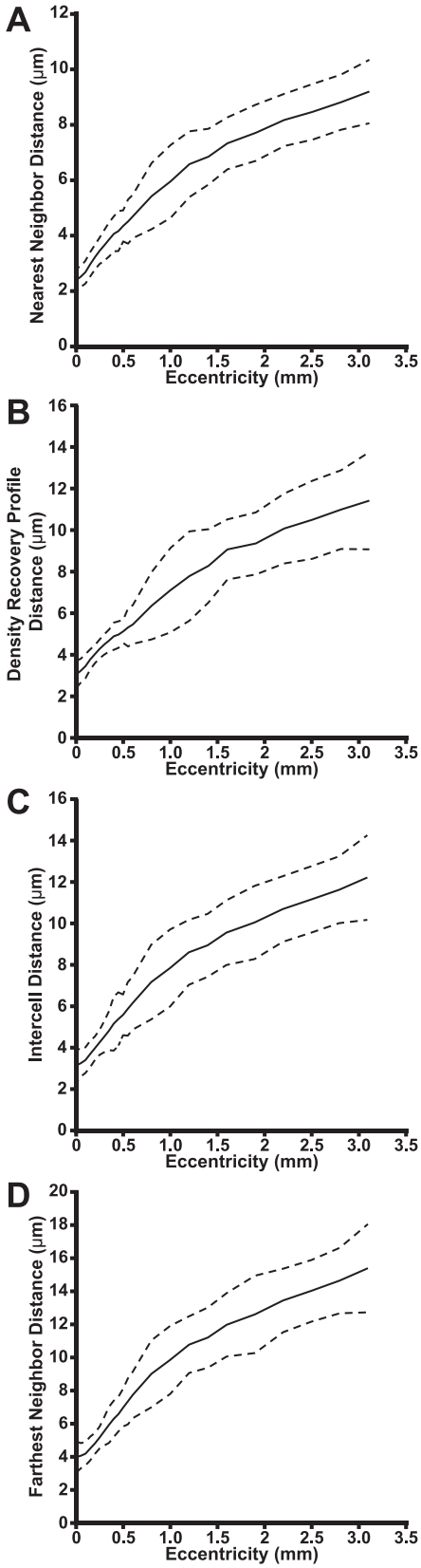

Figure 3. Mean population cone spacing measurements. Four different spacing measurements: (**A**) NND; (**B**) DRPD; (**C**) ICD; (**D**) FND are plotted as a function of eccentricity (*solid lines*) with their respective 95% prediction intervals (*dashed lines*). All four spacing metrics increased monotonically with eccentricity.

classifier, both the eccentricity of each ROI and the normal metric values from each subject were transformed to conform to statistical assumptions for linear models. Each ROI's eccentricity was transformed as follows:

$$E_t = \frac{1}{1 + E_{\mu m}}, \quad (1)$$

where $E_{\mu m}$ is eccentricity in μm, and E_t is the transformed eccentricity value. The metric values were transformed using the natural log. These transformed data were then fit to a polynomial (orders 1–4). The (1–4) polynomial coefficients from each fit were used to create a 95% prediction ellipsoid, which defined the plausible values for each coefficient.

We used this classifier to assess the sensitivity of each metric to undersampling with the following process: First, we randomly selected a subject and removed between 5% and 80% of the cone coordinates from each of their ROI's (again, representing diffuse cell loss due to disease, or cells missed during the identification step). Cones were removed by first permuting the cone coordinate list according to a uniform random distribution using the randperm MATLAB function. After permuting the cone coordinate list, the number of coordinates defined by the percent loss was removed from the beginning of the list. Next, the remaining (now undersampled) cone coordinates were analyzed using the metrics described above. We then transformed the resultant metric and eccentricity data and performed a polynomial fit as described above on these undersampled mosaics. Finally, we determined if the set of fit coefficients were significantly different from normal by comparing them with the prediction ellipsoid using Hotelling's *t*-squared statistic with a 95% significance cutoff.[53] This process was repeated 1000 times for each cone loss percentage to calculate an "abnormal mosaic detection rate."

Using this process, we assessed the detection rate of abnormalities (or statistical power) for each metric at different percent loss values. A metric was considered sensitive to loss at a given percent cone loss when it correctly identified abnormal mosaics in 80% of trials. Finally, at each eccentricity, we constructed 95% pointwise prediction intervals (PIs) for each of the above metrics to describe pointwise uncertainty.

Results

We were able to obtain images from all 20 subjects across each eccentricity. The numerical results are summarized in the Table (for meridian-specific values, refer to Supplementary Table S2). Figure 2A illustrates the expected exponential decrease of cone density with eccentricity as reported in previous studies,[5,19,20,51,52] and the 95% PI for our population. The PI appears larger near the foveal center due to the increased normal variability in foveal cone density. In contrast, the cone spacing metrics increased monotonically as a function of eccentricity (Fig. 3), with the 95% PI being smaller near the fovea (<500 μm). The three regularity metrics and percent six-sided cells followed previously observed patterns,[19,32–34] peaking at about 250 μm (Fig. 4).

To characterize how each metric was affected by undersampling, we first applied undersampling to a single ROI that exhibited average metric values (JC_10145, 200-μm eccentricity). Figure 5 illustrates the effect of 40% and 80% undersampling on this particular ROI. Qualitatively, the mosaic appears less regular with fewer cells remaining. However, without a priori eccentricity information, the ROI could simply be from a location more distant to the fovea. The histograms of each type of spacing each appear different; NND remains tightly clustered about the mean, whereas the mean and spread of ICD and FND measurements dramatically change as

Investigative Ophthalmology & Visual Science

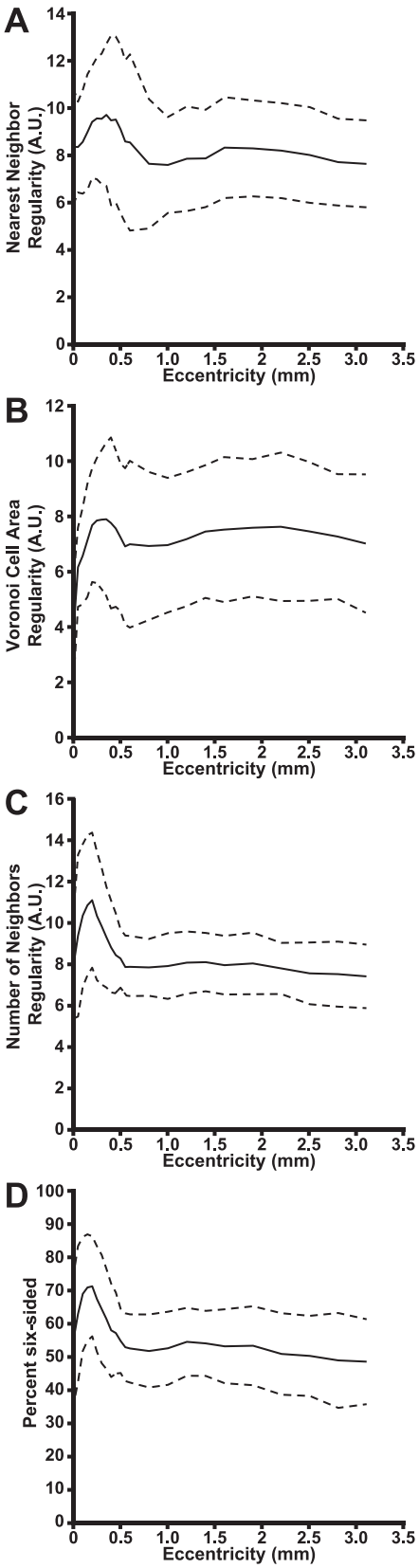

Figure 4. Mean population regularity measurements. Three different regularity measurements: (**A**) NNR; (**B**) VCAR; (**C**) Number of neighbors regularity and percent six-sided cells (**D**) are plotted as a function of eccentricity (*solid lines*) with their respective 95% prediction intervals (*dashed lines*). All three regularity metrics and percent six-sided cells increased in the parafoveal region and decreased near the foveal center.

increasing amounts of loss are applied. In the DRP, the mean only slightly changes; in fact, the estimated spacing decreased, though this is likely an artifact due to the bin size selection algorithm. All measurements of regularity and percent six-sided cells for this ROI decreased in response to undersampling (Fig. 6). In this single ROI, the percentage of six-sided cells decreased by a similar amount (by 39% between 0%–40% undersampling, by 40% between 40% and 80% undersampling) between each percent undersampling. Number of neighbors regularity decreased by 47% between 0% and 40% undersampling, and 32% between 40% and 80% undersampling. Interestingly, VCAR decreased by 75% between 0% and 40% undersampling, and roughly half that (31%) between 40% and 80% undersampling, implying that the metric changes more with lower amounts of loss. NNR was the opposite, decreasing only 27% between 0% and 40% undersampling, but substantially more (79%) between 40% and 80%.

We then used the prediction ellipse method described above to examine each metric's ability to detect undersampling in simulations from all 20 subjects. Density did not reliably detect an abnormality until 24% of the cones had been removed across all eccentricities (Fig. 2B). The NND and DRPD were remarkably insensitive to undersampling; an abnormal mosaic was unable to be detected for either metric until 53% and 55% of cone coordinates were removed, respectively (Fig. 7). In contrast, ICD and FND were able to detect an abnormal mosaic at 29% and 23% undersampling, respectively (Fig. 7). Of the regularity metrics, NNR was the least sensitive, and detected abnormality with above 35% undersampling (Fig. 7). The VCAR and percentage of six-sided cells and were similarly sensitive and were able to consistently detect a deviation from normal beyond 17% and 14% undersampling, respectively (Fig. 7). Of the regularity metrics, NoNR was the most sensitive, and was able to detect an abnormal mosaic after only 10% of the cone coordinates had been removed (Fig. 7).

Discussion

We characterized the normal cone mosaic as a function of eccentricity using both new and previously described geometrical metrics. The metrics examined here had different 95% PI widths, suggesting each metric had different variance. While we examined a wide variety of metrics describing the cone mosaic, this is not an exhaustive list; new metrics may be derived as other retinal cell types are imaged, or as disease processes are better understood. Additionally, metrics can be derived directly from the retinal image; approaches based on analysis of the Fourier spectrum of the image ("Yellot's Ring") are already in use,[12,25,26,29,30,37,42,54] and others have been published to assess beam direction in the lamina cribrosa.[55] Nevertheless, different metrics respond more sensitively to undersampling than others. NND, DRPD, and NNR were the least sensitive to cone undersampling, whereas percentage of six-sided Voronoi cells, VCAR, and NoNR were the most sensitive. Intuitively, one might think that the most sensitive metrics should always be used; however, there are some important points that should be reviewed to provide context to these results.

The pointwise PIs constructed here represent the range that individual metric values will fall, within 95% likelihood. The PIs are constructed from 20 subjects; assuming our 20 healthy subjects are representative of the variance in the population, our estimate of the PI is more conservative than it would be had we included a larger population. For each metric's PI, we aggregated the results from all meridians to construct the PI. In our population, metrics measured along each meridian (temporal, inferior, nasal, and superior) behaved similarly, which may not always hold.[52,56–58] In contrast, the

Investigative Ophthalmology & Visual Science

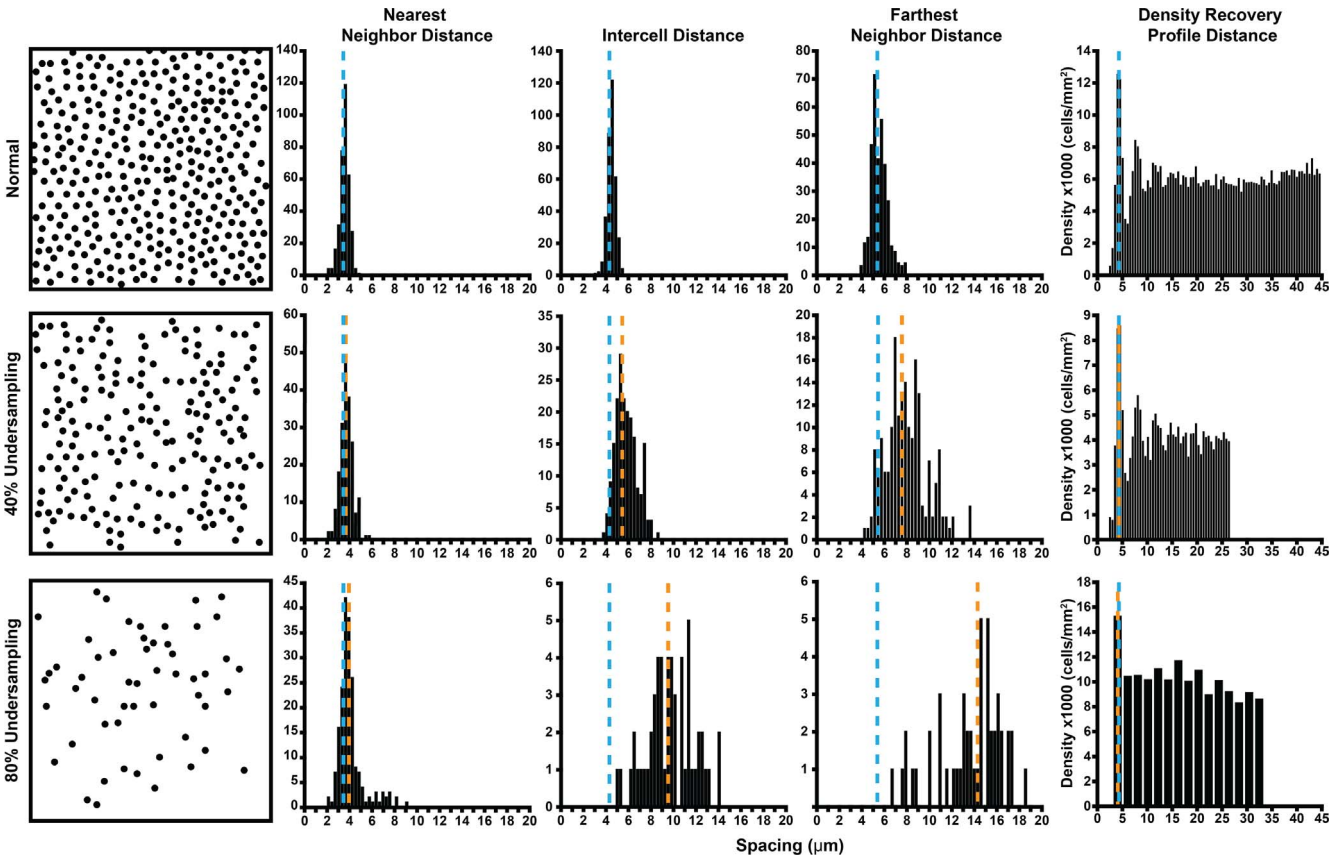

Figure 5. An illustration of the effect of cone undersampling on histograms of cell distances (NND, ICD, FND) and the DRPD from a single subject (JC_10145, image acquired 200 μm from the fovea). In each plot, the *blue dashed line* is the mean of the histogram from the complete mosaic, while the *orange dashed line* is the mean of the histograms from the 40% (*middle row*) and the 80% undersampled mosaics (*bottom row*). On all plots, the *y*-axis is the number of cells within each histogram bin. The NND histogram is only marginally affected (indicated by the similarity in the *blue and orange dashed lines*), even with an 80% loss. Similarly, the DRPD is largely unaffected by cell loss; its estimated spacing is only affected when the bin size increases (*bottom right*) due to a decrease in density. In contrast, the mean (indicated by further separation of the *blue and orange dashed lines*) and spread of both ICD and FND increase substantially with cell loss.

classifier tools were constructed for each metric to classify all ROIs from a single subject as either abnormal or normal. However, these classifiers were based on multiple regressions of our data. While density and spacing metrics fit lower order polynomial models closely (R^2 goodness-of-fit > 0.95), the unusual shape of the regularity metrics required higher-order (fourth) polynomials to fit well ($R^2 > 0.8$). While on average regularity metrics had R^2 goodness-of-fit values above 0.8, without a closer fit ($R^2 > 0.95$), our classifier may underestimate the true amount of variability in regularity metrics across all subjects.

In addition to affecting the size of the PI, the sample size can cause artifacts when constructing the statistical power curves. The prediction ellipse-based classifier used to generate the power curves is constructed from the normal data with no loss; thus, the classifier should correctly identify normal mosaics at a rate similar to the significance level of 95%, or statistical power of 5%.

A different issue relates to the type of cone loss that was adopted for these analyses. Photoreceptor loss is a dynamic process; when cones or rods die, their neighbors can move and fill the gaps, albeit to varying degrees.[22,39,59,60] This is seen in part in the image in Figure 8, which is from a subject with significant cone mosaic disruption (evidenced by the interleaved dark regions throughout the image).[38] The image has density and ICD values that correspond to only 48% of the normal mean at that eccentricity. However, the NND and DRPD values are

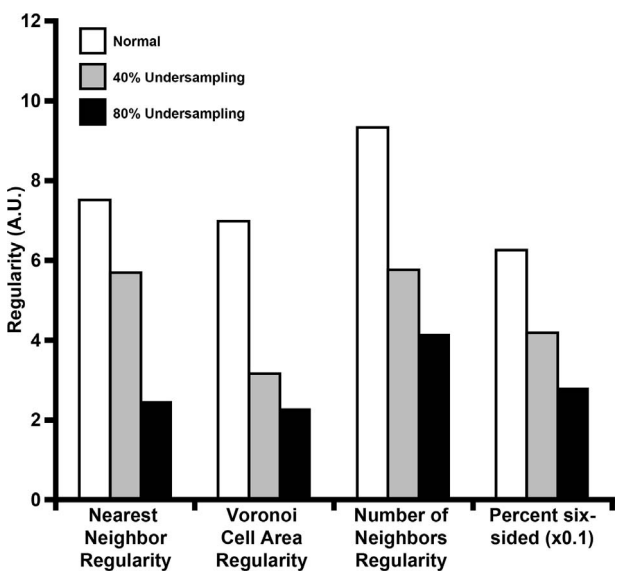

Figure 6. The effect of cone undersampling on measurements of regularity and percent six-sided cells in the same ROI shown in Figure 5. The measured value (normal) is represented by *white bars*. Undersampling the mosaic by 40% (*gray bars*) and 80% (*black bars*) results in a reduction in all four metrics, though each metric decreases at a different rate. Note: Percent six-sided cells has been divided by 10 to fit the scale.

Investigative Ophthalmology & Visual Science

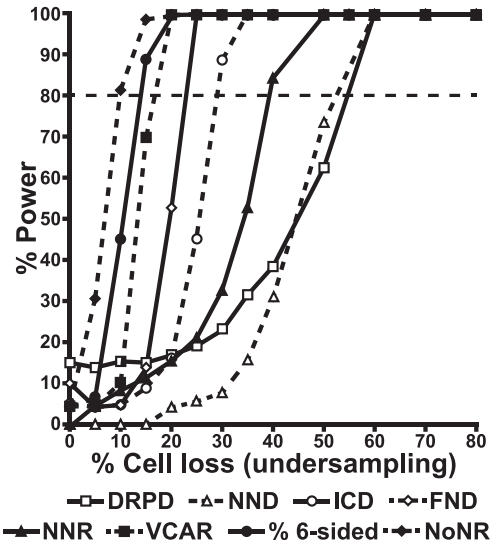

Figure 7. Statistical power curves (*solid lines*) for each metric as a function of the amount of undersampling (i.e., cell loss). The sensitivity of a given measurement was defined as the point at which the statistical power curve crossed 80% power (*horizontal dashed line*). Mean NND and DRPD are insensitive to cone undersampling and are only able to reliably detect cell loss when 53% and 55% of cone coordinates were removed, respectively. Mean ICD can reliably detect that the cone mosaic is abnormal after 29% of the cones were removed. Mean FND is the most sensitive of the four spacing metrics and is able to detect an abnormal mosaic after 23% of the cones were removed. Mean NNR was relatively insensitive and was unable to detect an abnormal mosaic until 40% of cones were removed. Percent six-sided cells and VCAR were able to detect abnormal mosaics with 17% and 14% undersampling, respectively. Mean NoNR was the most sensitive, detecting abnormal mosaics at 10% undersampling.

consistent with a greater than 70% cell loss, and VCAR, NoNR, and percent six-sided are consistent with only a 20% cell loss for this retinal location. Given that each of these metrics describe a different aspect of the mosaic, and that there is such a large disparity between the actual value of each metric and the value predicted by simulated undersampling, the inconsistency of these metrics is likely indicative of an alternative type of loss (such as photoreceptor remodeling). Regardless, exploring the relationship between different metrics and examining how each responds to both simulated and real loss could enable a more quantitative description of the type of cone loss in different retinal degenerations/loss types.

A major concern with the translation of AO imaging to the clinical arena (specifically clinical trials) is that image quality may not always be sufficient to visualize the entire photoreceptor mosaic. In addition to differences in hardware capabilities, pathologies such as AMD and RP are linked with poor image quality due to age or secondary effects of the disease (e.g., cataracts or cystoid macular edema).[61,62] In these situations, the use of a metric that is insensitive (i.e., robust) to undersampling (DRPD, NND, NNR) should be used. However, as shown here, these same metrics would be poorly suited for use in longitudinal studies, due to this very same insensitivity. Thus, one has to be very explicit with what it is they are trying to measure when choosing which metric to use. In the end, the most sensitive metric cannot be assumed to be the "best" metric.

Acknowledgments

The authors thank Alfredo Dubra, PhD, Mara Goldberg, Christopher Langlo, Erika Phillips, Moataz Razeen, MD, Phyllis Summerfelt, and Jonathon Young for their contributions.

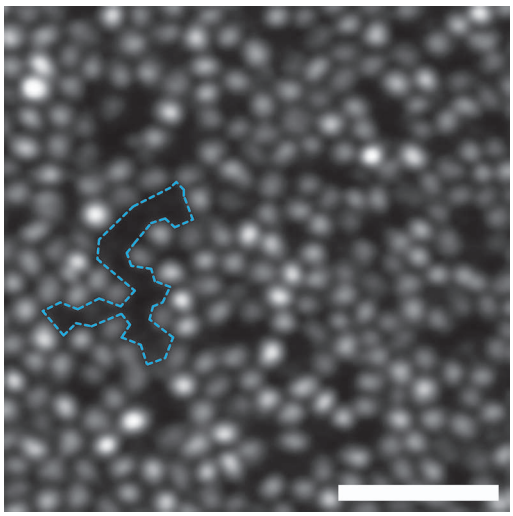

Figure 8. Evaluating metric performance in a real mosaic with cell loss. The images shown here are taken from a patient with a deutan color vision deficiency caused by the presence of a unique opsin haplotype encoded by their *OPN1MW* gene.[38] As can be seen in the image (acquired at 200 μm from the fovea), the cone mosaic has a diffuse loss of normal waveguiding cones (example region outlined in dotted cyan) that mimicks the simulated undersampling performed in the present study. Density and ICD were consistent with a simulated 48% undersampling. However, NND and density recovery profile distance were consistent with a greater than 70% simulated cell loss, and VCAR, number of neighbors regularity, and percent six-sided were consistent with only a 20% simulated cell loss at the same location. These findings illustrate that there has likely been reorganization of the mosaic in addition to discrete loss of waveguiding cones.

Supported in part by the National Center for Research Resources and the National Center for Advancing Translational Sciences of the National Institutes of Health under award number UL1TR001436 and by the National Eye Institute of the National Institutes of Health under award numbers P30EY001931, R01EY017607, and T32EY014537. Additional support was provided by Foundation Fighting Blindness (Columbia, MD, USA); The Edward N. & Della L. Thome Memorial Foundation, Bank of America, N.A. Trustee (Boston, MA, USA); the Gene & Ruth Posner Foundation (Milwaukee, WI, USA); and the Richard O. Schultz, MD/Ruth Works Professorship (Milwaukee, WI, USA). This investigation was conducted in part in a facility constructed with support from the Research Facilities Improvement Program; grant number C06RR016511 from the National Center for Research Resources, NIH.

Disclosure: **R.F. Cooper**, None; **M.A. Wilk**, None; **S. Tarima**, None; **J. Carroll**, None

References

1. Scoles D, Sulai YN, Langlo CS, et al. In vivo imaging of human cone photoreceptor inner segments. *Invest Ophthalmol Vis Sci*. 2014;55:4244–4251.
2. Williams DR. Imaging single cells in the living retina. *Vision Res*. 2011;51:1379–1396.
3. Miller DT, Kocaoglu OP, Wang Q, Lee S. Adaptive optics and the eye (super resolution OCT). *Eye*. 2011;25:321–330.
4. Liang J, Williams DR, Miller D. Supernormal vision and high-resolution retinal imaging through adaptive optics. *J Opt Soc Am A Opt Image Sci Vis*. 1997;14:2884–2892.
5. Zhang T, Godara P, Blancob ER, et al. Variability in human cone topography assessed by adaptive optics scanning laser ophthalmoscopy. *Am J Ophthalmol*. 2015;160:290–300.

6. Dubra A, Sulai Y, Norris JL, et al. Noninvasive imaging of the human rod photoreceptor mosaic using a confocal adaptive optics scanning ophthalmoscope. *Biomed Opt Express*. 2011; 2:1864–1876.
7. Merino D, Duncan JL, Tiruveedhula P, Roorda A. Observation of cone and rod photoreceptors in normal subjects and patients using a new generation adaptive optics scanning laser ophthalmoscope. *Biomed Opt Express*. 2011;2:2189–2201.
8. Rossi EA, Chung M, Dubra A, Hunter JJ, Merigan WH, Williams DR. Imaging retinal mosaics in the living eye. *Eye*. 2011;25: 301–308.
9. Scoles D, Sulai YN, Dubra A. In vivo dark-field imaging of the retinal pigment epithelium cell mosaic. *Biomed Opt Express*. 2013;4:1710–1723.
10. Morgan JIW, Hunter JJ, Masella B, et al. Light-induced retinal changes observed with high-resolution autofluorescence imaging of the retinal pigment epithelium. *Invest Ophthalmol Vis Sci*. 2008;49:3715–3729.
11. Torti C, Považay B, Hofer B, et al. Adaptive optics optical coherence tomography at 120,000 depth scans/s for non-invasive cellular phenotyping of the living human retina. *Opt Express*. 2009;17:19382–19400.
12. Roorda A, Zhang Y, Duncan JL. High-resolution in vivo imaging of the RPE mosaic in eyes with retinal disease. *Invest Ophthalmol Vis Sci*. 2007;48:2297–2303.
13. Morgan JIW, Dubra A, Wolfe R, Merigan WH, Williams DR. In vivo autofluorescence imaging of the human and macaque retinal pigment epithelial cell mosaic. *Invest Ophthalmol Vis Sci*. 2009;50:1350–1359.
14. Chiu SJ, Lokhnygina Y, Dubis AM, et al. Automatic cone photoreceptor segmentation using graph theory and dynamic programming. *Biomed Opt Express*. 2013;4:924–937.
15. Garrioch R, Langlo C, Dubis AM, Cooper RF, Dubra A, Carroll J. Repeatability of in vivo parafoveal cone density and spacing measurements. *Optom Vis Sci*. 2012;89:632–643.
16. Li KY, Tiruveedhula P, Roorda A. Intersubject variability of foveal cone photoreceptor density in relation to eye length. *Invest Ophthalmol Vis Sci*. 2010;51:6858–6867.
17. Song H, Chui TY, Zhong Z, Elsner AE, Burns SA. Variation of cone photoreceptor packing density with retinal eccentricity and age. *Invest Ophthalmol Vis Sci*. 2011;52:7376–7384.
18. Chui TYP, Song HX, Burns SA. Individual variations in human cone photoreceptor packing density: variations with refractive error. *Invest Ophthalmol Vis Sci*. 2008;49:4679–4687.
19. Dees EW, Dubra A, Baraas RC. Variability in parafoveal cone mosaic in normal trichromatic individuals. *Biomed Opt Express*. 2011;2:1351–1358.
20. Lombardo M, Lombardo G, Schiano Lomoriello D, Ducoli P, Stirpe M, Serrao S. Interocular symmetry of parafoveal photoreceptor cone density. *Retina*. 2013;33:1640–1649.
21. Flatter JA, Cooper RF, Dubow MJ, et al. Outer retinal structure after closed-globe blunt ocular trauma. *Retina*. 2014;34:2133–2146.
22. Hansen SO, Cooper RF, Dubra A, Carroll J, Weinberg DV. Selective cone photoreceptor injury in acute macular neuroretinopathy. *Retina*. 2013;33:1650–1658.
23. Park SP, Chung JK, Greenstein V, Tsang SH, Chang S. A study of factors affecting the human cone photoreceptor density measured by adaptive optics scanning laser ophthalmoscope. *Exp Eye Res*. 2013;108:1–9.
24. Menghini M, Lujan BJ, Zayit-Soudry S, et al. Correlation of outer nuclear layer thickness with cone density values in patients with retinitis pigmentosa and healthy subjects. *Invest Ophthalmol Vis Sci*. 2015;56:372–381.
25. Duncan JL, Zhang Y, Gandhi J, et al. High-resolution imaging with adaptive optics in patients with inherited retinal degeneration. *Invest Ophthalmol Vis Sci*. 2007;48:3283–3291.
26. Roorda A, Metha AB, Lennie P, Williams DR. Packing arrangement of the three cone classes in primate retina. *Vision Res*. 2001;41:1291–1306.
27. Roorda A, Romero-Borja F, Donnelly WJ III, Queener H, Hebert T, Campbell M. Adaptive optics scanning laser ophthalmoscopy. *Opt Express*. 2002;10:405–412.
28. Ratnam K, Carroll J, Porco TC, Duncan JL, Roorda A. Relationship between foveal cone structure and clinical measures of visual function in patients with inherited retinal degenerations. *Invest Ophthalmol Vis Sci*. 2013;54:5836–5847.
29. Syed R, Sundquist SM, Ratnam K, et al. High-resolution images of retinal structure in patients with choroideremia. *Invest Ophthalmol Vis Sci*. 2013;54:950–961.
30. Yoon MK, Roorda A, Zhang Y, et al. Adaptive optics scanning laser ophthalmoscopy images in a family with the mitochondrial DNA T8993C mutation. *Invest Ophthalmol Vis Sci*. 2009; 50:1838–1847.
31. Mkrtchyan M, Lujan BJ, Merino D, Roorda A, Duncan JL. Outer retinal structure in patients with acute zonal occult outer retinopathy. *Am J Ophthalmol*. 2012;153:757–768.
32. Baraas RC, Carroll J, Gunther KL, et al. Adaptive optics retinal imaging reveals S-cone dystrophy in tritan color-vision deficiency. *J Opt Soc Am A Opt Image Sci Vis*. 2007;24: 1438–1447.
33. Carroll J, Rossi EA, Porter J, et al. Deletion of the X-linked opsin gene array locus control region (LCR) results in disruption of the cone mosaic. *Vision Res*. 2010;50:1989–1999.
34. Li KY, Roorda A. Automated identification of cone photoreceptors in adaptive optics retinal images. *J Opt Soc Am A Opt Image Sci Vis*. 2007;24:1358–1363.
35. Cook JE. Spatial properties of retinal mosaics: an empirical evaluation of some existing measures. *Vis Neurosci*. 1996;13: 15–30.
36. Rodieck RW. The density recovery profile: a method for the analysis of points in the plane applicable to retinal studies. *Vis Neurosci*. 1991;6:95–111.
37. Cooper RF, Langlo CS, Dubra A, Carroll J. Automatic detection of modal spacing (Yellott's ring) in adaptive optics scanning light ophthalmoscope images. *Ophthalmic Physiol Opt*. 2013; 33:540–549.
38. Carroll J, Neitz M, Hofer H, Neitz J, Williams DR. Functional photoreceptor loss revealed with adaptive optics: an alternate cause of color blindness. *Proc Natl Acad Sci U S A*. 2004;101: 8461–8466.
39. Carroll J, Baraas RC, Wagner-Schuman M, et al. Cone photoreceptor mosaic disruption associated with Cys203Arg mutation in the M-cone opsin. *Proc Natl Acad Sci U S A*. 2009; 106:20948–20953.
40. Choi SS, Doble N, Hardy JL, et al. In vivo imaging of the photoreceptor mosaic in retinal dystrophies and correlations with visual function. *Invest Ophthalmol Vis Sci*. 2006;47: 2080–2092.
41. Sun LW, Johnson RD, Langlo C, et al. Assessing photoreceptor structure in retinitis pigmentosa and Usher syndrome. *Invest Ophthalmol Vis Sci*. 2016;57:2428–2442.
42. Ratnam K, Västinsalo H, Roorda A, Sankila E-MK, Duncan JL. Cone structure in patients with Usher syndrome type III and mutations in the *Clarin 1* gene. *JAMA Ophthalmol*. 2013;131: 67–74.
43. Miller DT, Williams DR, Morris GM, Liang J. Images of cone photoreceptors in the living human eye. *Vision Res*. 1996;36: 1067–1079.
44. Wade AR, Fitzke FW. In vivo imaging of the human cone photoreceptor mosaic using a confocal laser scanning ophthalmoscope. *Lasers Light Ophthalmol*. 1998;8:129–136.

Investigative Ophthalmology & Visual Science

45. Wolsley CJ, Saunders KJ, Silvestri G, Anderson RS. Comparing mfERGs with estimates of cone density from in vivo imaging of the photoreceptor mosaic using a modified Heidelberg retina tomograph. *Vision Res*. 2010;50:1462–1468.
46. Larocca F, Nankivil D, Farsiu S, Izatt JA. Handheld simultaneous scanning laser ophthalmoscopy and optical coherence tomography system. *Biomed Opt Express*. 2013;4:2307–2321.
47. Bennett AG, Rudnicka AR, Edgar DF. Improvements on Littmann's method of determining the size of retinal features by fundus photography. *Graefe's Arch Clin Exp Ophthalmol*. 1994;232:361–367.
48. Dubra A, Sulai Y. Reflective afocal broadband adaptive optics scanning ophthalmoscope. *Biomed Opt Express*. 2011;2:1757–1768.
49. Dubra A, Harvey Z. Registration of 2D images from fast scanning ophthalmic instruments. In: Fischer B, Dawant B, Lorenz C, eds. *Lecture Notes in Computer Science*. Berlin, Germany: Springer-Verlag; 2010;60–71.
50. Putnam NM, Hofer HJ, Doble N, Chen L, Carroll J, Williams DR. The locus of fixation and the foveal cone mosaic. *J Vis*. 2005;5(7):3.
51. Wilk MA, McAllister JT, Cooper RF, et al. Relationship between foveal cone specialization and pit morphology in albinism. *Invest Ophthalmol Vis Sci*. 2014;55:4186–4198.
52. Curcio CA, Sloan KR, Kalina RE, Hendrickson AE. Human photoreceptor topography. *J Comp Neurol*. 1990;292:497–523.
53. Hotelling H. The generalization of student's ratio. *The Annals of Mathmatical Statistics*. 1931;2:360–378.
54. Roorda A, Williams DR. Optical fiber properties of individual human cones. *J Vis*. 2002;2(5):4.
55. Sredar N, Ivers KM, Queener HM, Zouridakis G, Porter J. A principal component analysis based approach to determine predominant lamina cribrosa beam orientation directly from in vivo images. *J Vis*. 2013;13(15):71.
56. Curcio CA, Sloan KR. Packing geometry of human cone photoreceptors: Variation with eccentricity and evidence for local anisotropy. *Vis Neurosci*. 1992;9:169–180.
57. Curcio CA, Sloan KR Jr, Packer O, Hendrickson AE, Kalina RE. Distribution of cones in human and monkey retina: individual variability and radial symmetry. *Science*. 1987;236:579–582.
58. Chui TYP, Song H, Burns SA. Adaptive-optics imaging of human cone photoreceptor distribution. *J Opt Soc Am A Opt Image Sci Vis*. 2008;25:3021–3029.
59. Cideciyan AV, Hufnagel RB, Carroll J, et al. Human cone visual pigment deletions spare sufficient photoreceptors to warrant gene therapy. *Hum Gene Ther*. 2013;24:993–1006.
60. Curcio CA. Photoreceptor topography in ageing and age-related maculopathy. *Eye*. 2001;15:376–383.
61. Talcott KE, Ratnam K, Sundquist S, et al. Longitudinal study of cone photoreceptors during retinal degeneration and in response to ciliary neurotrophic factor treatment. *Invest Ophthalmol Vis Sci*. 2011;52:2219–2226.
62. Land ME, Cooper RF, Young J, et al. Cone structure in subjects with known genetic relative risk for AMD. *Optom Vis Sci*. 2014;91:939–949.

Investigative Ophthalmology & Visual Science